Influence of Photochemical Loss of VOCs on Understanding Ozone Formation Mechanism

Wei Ma[1], Zemin Feng[1,7], Junlei Zhan[1], Yongchun Liu[1*], Pengfei Liu[2,4,5], Chengtang Liu[2,4,5], Qingxin

Ma[2,4,5], Kang Yang[3], Yafei Wang[3], Hong He[2,4,5], Markku Kulmala[1,6], Yujing Mu[2,4,5], Junfeng Liu[2,4,5*]

1. Aerosol and Haze Laboratory, Advanced Innovation Center for Soft Matter Science and Engineering,

Beijing University of Chemical Technology, Beijing, 100029, China

2. Research Center for Eco-Environmental Sciences, Chinese Academy of Sciences, Beijing, 100085, China

3. Beijing Institute of Petrochemical Technology, Beijing 102617, China

4. Center for Excellence in Regional Atmospheric Environment, Institute of Urban Environment, Chinese

Academy of Sciences, Xiamen 361021, China

5. University of Chinese Academy of Sciences, Beijing 100049, China

6. Institute for Atmospheric and Earth System Research, Faculty of Science, University of Helsinki, Helsinki,

00014, Finland

7. College of Chemical Engineering, North China University of Science and Technology, Tangshan 063021,

China.

*Corresponding to: Yongchun Liu (liuyc@buct.edu.cn) and Junfeng Liu (junfengliu@rcees.ac.cn)

Abstract

Volatile organic compounds (VOCs) tend to be consumed by atmospheric oxidants, resulting in substantial photochemical loss during transport. An observation-based model was used to evaluate the influence of photochemical loss of VOCs on the sensitivity regime and mechanisms of ozone formation. Our results showed that a VOC-limited regime based on observed VOC concentrations shifted to a transition regime with a photochemical initial concentration of VOCs (PIC-VOCs) in the morning. The net ozone formation rate was underestimated by 3 ppb h^{-1} (~36 ppb day^{-1}) based on the PIC-VOCs. The relative contribution of the RO_2 path to ozone production based on the PIC-VOCs accordingly increased by 13.4%; in particular, the contribution of alkene-derived RO_2 increased by approximately 10.2%. In addition, the OH-HO_2 radical cycle was obviously accelerated by highly reactive alkenes after accounting for photochemical loss of VOCs. The contribution of local photochemistry might be underestimated for both local and regional ozone pollution if consumed VOCs are not accounted for, and policymaking on ozone pollution prevention should focus on VOCs with a high reactivity.

1. Introduction

Ground surface ozone (O_3) is an important atmospheric pollutant that is harmful to human health and is connected with respiratory, cardiovascular diseases, and premature mortality (Cohen et al., 2017). It is also harmful to vegetation growth. For example, it led to annual reductions in the yields of rice and wheat by 8% and 6%, respectively, and reduced forest biomass growth by 11-13% in China (Feng et al., 2019). Surface O_3 concentrations have increased by 11.9% over eastern China despite the air pollution control measures implemented in China from 2012 to 2017 (Dang and Liao, 2019). An economic loss of 0.09% of the Chinese gross domestic product (78 billion CNY) is predicted for 2030 if policies against O_3 pollution are not properly implemented (Xie et al., 2019). Therefore, urgent action to minimize O_3 pollution in China is needed.

Tropospheric O_3 is mainly produced from photochemical reactions between volatile organic compounds (VOCs) and nitrogen oxides (NO_x: $NO+NO_2$) (Seinfeld and Pandis, 2006; Liu et al., 2021). O_3 is generated from a collision of O_2 and $O(3P)$ that is produced from photolysis of NO_2 in the atmosphere. Peroxyl radicals (HO_2 and RO_2), which are produced from the oxidation of VOCs by OH radical, can efficiently convert NO (from the photolysis of NO_2) to NO_2, leading to a net O_3 production by compensating for the titration of O_3 by NO (Monks, 2005; Zhang et al., 2021a). Over the past two decades, a number of field observations focused on O_3 pollution levels and its precursors have been carried out in the Beijing-Tianjin-Hebei (BTH), Yangtze River Delta (YRD), and Pearl River Delta (PRD) regions (Wang et al., 2017; Li et al., 2019; Xue et al., 2014; Zhang et al., 2019). Due to the nonlinear relationship

3

55   between O_3 and its precursors and the variations in meteorological conditions, numerous

56   studies have been performed to understand the sensitivity regime of O_3 formation (Ling and

57   Guo, 2014; Zhang et al., 2020), the photochemical process of O_3 formation based on box

58   models or observation-based models (OBM) (He et al., 2019; Tan et al., 2019), and the sources

59   of O_3 using regional chemical transport models (Li et al., 2016b; Li et al., 2016c). Recently,

60   the instantaneous production rate of the O_3 formation process has attracted more attention; for

61   example, studies examining radical recycling (OH-RO_2-RO-HO_2-OH) related to the production

62   of O_3 have been performed (Lu et al., 2017; Tan et al., 2017; Whalley et al., 2018). HCHO

63   photolysis and alkene ozonolysis contributed approximately 85% to the primary production of

64   HO_2 and HO radicals in Beijing, Shanghai and Guangzhou (Tan et al., 2019; Yang et al., 2017).

65   The importance of HONO and HCHO photolysis for primary radical production has also been

66   proposed in suburban and rural areas (Tan et al., 2017; Lu et al., 2012; Lu et al., 2013).

67   All of the OBM studies investigating the relationship between O_3 and VOCs were based

68   on measured datasets. However, VOCs are highly reactive to atmospheric oxidants, such as

69   OH, NO_3, and O_3, among which OH is dominant. The lifetimes of some highly reactive VOCs,

70   such as isoprene, are as short as only a few tens of minutes under typical daytime atmospheric

71   conditions. The mixing ratios of VOCs observed at a sampling site are actually the residues of

72   VOCs from emissions due to the photochemical loss during transport from the source site to

73   the receptor site. If photochemically consumed VOCs are not considered, the O_3 formation

74   sensitivity and net O_3 production may be misunderstood, and subsequent policymaking on O_3

75   pollution prevention at regional or urban scales may be misguided. Thus, the photochemical

76   age-based approach has been applied to evaluate the effect of photochemical processes on VOC

77   measurements (Shao et al., 2011). This method was used to qualitatively or semi-quantitatively

78   estimate the O_3 formation process of the source-receptor (Gao et al., 2018) by calculating the

79   O_3 formation potential (OFP) (Han et al., 2017), identifying the critical species for O_3 formation

80   (Gao et al., 2021), or evaluating the VOC emissions ratio (Yuan et al., 2013). In evaluating the

81   importance of initial VOCs to ozone production, Xie et al. (2008) found that the OFP at a

82   Peking University site increased by 70% after accounting for the photochemical loss of VOCs.

83   Li et al. (2015) also showed that the OFPs of total NMHCs (excluding isoprene) increased by

84   16.1% (from 59.6 to 69.2 ppb O_3), 12.1% (from 33.5 to 37.5 ppb O_3), and 3.4% (from 68.9 to

85   71.2 ppb O_3) after correcting for photochemical loss in Gucheng, Quzhou, and Beijing,

86   respectively. Gao et al. (2018) reported that the OFP could be underestimated by 23.4% (62.4

87   ppb O_3) in Beijing if the photochemical loss of VOCs is not considered. Zhan et al. (2021)

88   found that based on measured VOCs, the OFP increased from 57.8 ppb to 103.9 ppb using the

89   initial VOCs. All the previous work was based on the maximum incremental reactivities (MIR)

90   method. The application of such calculations using the MIR method is restricted to areas or

91   episodes in which O_3 formation is VOC-sensitive (Carter, 1994). In the troposphere, the

92   sensitivity of ozone formation to NOx and VOCs varies greatly, as evidenced by the wide range

93   of OFP underestimations from ~3% to 70% in previous work. In addition, the MIR values of

94   VOC species for a specific region are calculated with the base scenario, in which NO

95   concentration and other parameters are the values that correspond to the maximal incremental

96   reactivity (IR). The fixed MIR values of different VOCs can neither reflect the non-linear

97 relationship between ozone and VOCs, involving in the complicated radical recycling (OH-

98 RO_2-RO-HO_2-OH) related to the production of ozone, nor be used for analyzing the radical

99 budget of the initial VOCs concentration. Thus, a quantitative analysis is necessary to explicitly

100 understand the influence of photochemical loss of VOCs on ozone formation and its

101 mechanism based on OBM studies, in which the dynamic atmospheric and meteorological

102 conditions is accounted for.

103   In this study, an OBM was used to evaluate the local O_3 formation process in summer in

104 Beijing based on concentrations of observed and photochemical initial concentrations of VOCs

105 (PIC-VOCs). The O_3-NOx-VOC sensitivity, instantaneous O_3 formation rate and in situ O_3

106 formation process were discussed. The aim of this study was to understand the possible

107 influence of photochemical loss of VOCs on the formation sensitivity regime of O_3 and how

108 the photochemical loss of VOCs affects O_3 formation. This study can provide new insight for

109 better understanding atmospheric O_3 pollution.

2. Methodology

2.1 Experimental section

112   Field observations were carried out on the Qingyuan campus of the Beijing Institute of

113 Petrochemical Technology (BIPT, 39.73°N and 116.33°E) (Figure S1). Details on the

114 observation site have been described in our previous work (Zhan et al., 2021). In short, the site

115 is a typical suburban site in the Daxing District between 5th Ring Road and 6th Ring Road. The

116 field campaign was carried out during August 1-28, 2019, when photochemistry was the most

117 active and rainfall was rare in Beijing.

118   The concentrations of nonmethane hydrocarbons (NMHCs) were detected by both a gas

119   chromatography-flame ionization detector (GC/FID) and a single photon ionization (SPI) TOF-

120   MS (SPI-MS 3000, Guangzhou Hexin Instrument Co., Ltd., China). A detailed description of

121   the instrumentation can be found in previous publications (Zhan et al., 2021; Chen et al., 2020).

122   The SPI-MS was also used to detect halohydrocarbons. More details on this instrument and its

123   parameter settings have been described in previous studies (Zhang et al., 2019; Liu et al.,

124   2020a). In short, a 0.002 int thick polydimethylsiloxane (PDMS) membrane (Technical

125   Products Inc., USA) was used to collect VOCs and diffuse them from the sample site to the

126   detector under high vacuum conditions. Vacuum ultraviolet (VUV) light generated by a

127   commercial D2 lamp (Hamamatsu, Japan) was utilized for ionization at 10.8 eV. For ion

128   detection, two microchannel plates (MCPs, Hamamatsu, Japan) assembled with a chevron-type

129   configuration were employed. This TOF-MS has an LOD varying from 50 ppt to 1 ppb with a

130   1-minute time resolution for most trace gases without any preconcentration procedure. To

131   verify the data compatibility of the SPIMS and GC/FID, we compared the concentrations of

132   toluene measured using these two different instruments (Figure S2). The correlation coefficient

133   was 0.9 (with a slope of 0.7), indicating that the concentrations of NMHCs were comparable

134   using these two measurement techniques.

135   Oxygenated VOCs (OVOCs) were collected using 2,4-dinitrophenylhydrazine (DNPH)-

136   coated silica gel cartridges (Sep-Pak, Waters) by an automatic sampling device with a sampling

137   flow rate of 1.2 L min^{-1} and a duration of 2 h for each sample. Then, the OVOCs were analysed

138   using high-performance liquid chromatography (HPLC, Inertsil ODS-P 5 μm 4.6 × 250 mm

139   column, GL Sciences) with an acetonitrile-water binary mobile phase (Ma et al., 2019). To

140   avoid possible contamination or desorption after sampling, cartridges were capped, placed into

141   tightly closed plastic bags and kept in a refrigerator before analysis. The sampled cartridges

142   were eluted with 5 mL acetonitrile and analysed by HPLC as soon as possible after they were

143   shipped back to the laboratory. This system was calibrated with 8-gradient standard solutions

144   (TO11/IP-6A Aldehyde/Ketone-DNPH Mix, SUPELCO). The correlation coefficients were all

145   greater than 0.999. The LOD for most OVOCs was approximately 10 ppt.

146   Trace gases, including NO_x, SO_2, CO, and O_3, were measured using corresponding

147   analysers (Thermo Scientific, 42i, 43i, 48i, and 49i, respectively). The HONO concentration

148   was measured using a homemade long path absorption photometer (LOPAP) (Liu et al., 2020c).

149   The meteorological parameters, including temperature (T), pressure (P), relative humidity

150   (RH), wind speed, and wind direction, were measured by a weather station (AWS310, Vaisala).

151   The photolysis rate (J_{NO2}) was measured via continuous measurement of the actinic flux in the

152   wavelength range of 285-375 nm using a J_{NO2} filter radiometer (J_{NO2} radiometer, Metcon).

153   **2.2 Calculation of photochemical loss of VOCs**

154   The photochemical loss of VOCs was calculated using the ratio method (Wiedinmyer et

155   al., 2001; Yuan et al., 2013). The initial mixing ratio of a specific VOC was calculated using

156   the following equations (Mckeen et al., 1996):

157   $$[VOC_i]_t = [VOC_i]_{t0} \times \exp(-k_i \times [OH] \times \Delta t) \quad (1)$$

158   $$\Delta t = \frac{1}{[OH] \times (k_X - k_E)} \times \left\{ ln\left(\frac{X_0}{E_0}\right) - ln\left(\frac{X_t}{E_t}\right) \right\} \quad (2)$$

159   where $[VOC_i]_t$ and $[VOC_i]_{t0}$ are the observed and initial concentrations of VOC_i, respectively;

160   k_i is the second-order reaction rate between compound i and OH radical; and $[OH]$ and Δt are

161   the concentration of OH radical and the photochemical ageing time, respectively. k_X and k_E are

162   rate constants for the reaction between OH radicals and ethylbenzene (7.00×10^{-12} cm^3

163   molecule^{-1} s^{-1}) and xylene (1.87×10^{-11} cm^3 molecule^{-1} s^{-1}) (Atkinson and Arey, 2003),

164   respectively. (X_0/E_0) is the initial mixing ratio between xylene and ethylbenzene, and (X_t/E_t) is

165   the mixing ratio between xylene and ethylbenzene at the observation time. In this study, we

166   chose the mean concentrations of xylene and ethylbenzene at 05:00-06:00 as their initial

167   concentrations before sunrise according to the ambient J_{NO2} (Figure S3) to calculate the

168   photochemical loss of OH exposure. In previous work (Shao et al., 2011; Zhan et al., 2021),

169   the selection of ethylbenzene and xylene as tracers was justified for calculating ambient OH

170   exposure under the following conditions: 1) the concentrations of xylene and ethylbenzene

171   were well correlated (Figure S4), which indicated that they were simultaneously emitted; 2)

172   they had different degradation rates in the atmosphere; and 3) the calculated PICs were in good

173   agreement with those calculated using other tracers, such as i-butene/propene (Figure S5)

174   (Zhan et al., 2021). To test the relative constant emission ratio from different sources, we chose

175   benzene vs. acetylene and n-hexane vs. toluene as references, and the result is shown in Figure

176   S6. These ambient ratios could directly reflect their relative emission rates from sources

177   (Goldan et al., 2000; Jobson et al., 2004). The linear correlation coefficients (R^2) were generally

178   higher than 0.7, which were equal to that reported by Shao et al. (2011). To further test the

179   assumption that the emissions of xylene and ethylbenzene were constant throughout the day,

180   their potential sources were calculated using a source-receptor model (the potential source

181   contribution function, PSCF). As shown in Figure S7, xylene and ethylbenzene showed similar

182   distributions. In addition, the ratio of ethylbenzene/xylene at 5:00 and 6:00 was similar to that

183   during the daytime. These results indicated that the emissions of xylene and ethylbenzene were

184   constant throughout the day. The ratio of xylene to ethylbenzene and the OH exposure

185   concentration are shown in Figure S8. The results showed that the ratio of xylene to

186   ethylbenzene increased gradually (07:00~12:00), which is consistent with the trend of xylene

187   and ethylbenzene. The OH exposure was from 0.82 to 8.1×10^6 molecule cm^{-3} h, with a mean

188   daytime value of $4.3 \pm 1.9 \times 10^6$ molecules cm^{-3} h. Accordingly, the mean photochemical ages

189   were 1.7 ± 0.9 h using the mean daytime (8:00-17:00 LT) OH concentrations ($4.3 \pm 3.1 \times 10^6$

190   molecules cm^{-3}) calculated based on JO1D using the method reported in our previous work

191   (Liu et al., 2020b; Liu et al., 2020c). This meant that VOCs would undergo obvious degradation

192   even during a short range of transport in the atmosphere.

193   It should be noted that the k_{OH} of isoprene is 9.98×10^{-11} cm^3 $molecule^{-1}$ s^{-1} at 298.15 K

194   (Atkinson and Arey, 2003), almost two orders of magnitude greater than other VOCs. The ratio

195   method assumes constant emissions for VOCs. However, the emission of isoprene greatly

196   depends on temperature and solar irradiation intensity (Zhang et al., 2021b). In addition to

197   accounting for photochemical loss, additional correction of daytime isoprene concentrations

198   was performed using the average diurnal flux of isoprene emissions (Figure S9 (Zhang et al.,

199   2021b). The emission of isoprene showed a clear unimodal curve, and the volume

200   concentration of isoprene was calculated based on the daily emission curve using Eq. (S1).

201 **2.3 Observation-based model simulation**

202   A box model based on the Master Chemical Mechanism (MCM3.3.1) and the Regional

203 Atmospheric Chemical Mechanism (RACM2) was used in this study. The MCM3.3.1 was used

204 to understand the instantaneous ozone formation process, and the RACM2 was used to depict

205 the ozone isopleth due to its high computational efficiency (Sect. 2.4). Table S1 shows the

206 model inputs. The model calculations were constrained with the measured meteorological

207 parameters (RH, T, P, and J_{NO2}) and the concentrations of trace gases, including inorganic

208 species (NO, NO_2, CO, SO_2, and HONO) and 61 organic species (NMHCs (46), OVOCs (8),

209 and halohydrocarbons (7)). The model was validated using the observed and simulated O_3

210 concentrations, which showed good consistency, as shown in Figure S10. The slope and

211 correlation coefficients were 0.9 and 0.8, respectively (Figure S11, respectively, indicating the

212 validity of the model simulation. It is worth mentioning that the results of model simulation

213 can sometimes be overestimated or underestimated to some extent, which has also been

214 reported by previous studies (Zong et al., 2018; Zhang et al., 2020), but this did not affect our

215 simulations of the ozone formation process and mechanisms because we constrained the ozone

216 concentration during our simulations.

217   The ozone formation rate P(O_3) can be quantified by the oxidation rate of NO to NO_2 by

218 peroxyl radicals (Tan et al., 2019), as expressed in Eq. (3). In this study, the modelled peroxyl

219 radical concentrations were used to calculate the ozone production rate.

220 $$P(O_3) = k_{HO_2+NO}[HO_2][NO] + k_{RO_2+NO}[RO_2][NO] \quad (3)$$

221 where $P(O_3)$ is the ozone formation rate; $[HO_2]$ and $[RO_2]$ are the number concentrations of

222   *HO_2 and RO_2 radicals; k_{HO2+NO} is the second reaction rate between HO_2 and NO; and k_{RO2+NO}*

223   *is the second reaction rate for the reaction of RO_2 and NO, which only produces RO and NO_2.*

224   Once ozone forms, it will be consumed by OH, HO_2, and alkenes. Additionally, some NO_2 can

225   react with OH, resulting in the formation of nitrate before photolysis. The chemical loss of both

226   O_3 and NO_2 is considered in the calculation of the net ozone production rate (Tan et al., 2019),

227
$$L(O_3) = \left(k_{O_3+OH}[OH] + k_{O_3+HO_2}[HO_2] + k_{O_3+alkenes}[alkenes]\right)[O_3] +$$

228
$$k_{NO_2+OH}[NO_2][OH] \quad (4)$$

229   where $L(O_3)$ is the ozone chemical loss rate; $[OH]$ is the number concentration of OH radical;

230   k_{O3+OH}, k_{O3+HO2}, and $k_{O3+alkenes}$ are the second-order reaction rate constants between O_3 and OH,

231   HO_2 and alkenes, respectively; and k_{NO2+OH} is the second-order reaction rate constant between

232   NO_2 and OH. Finally, $F(O_3)$ is the net ozone formation rate calculated by the difference between

233     $P(O_3)$ and $L(O_3)$, as expressed in Eq. (5),

234
$$F(O_3) = P(O_3) - L(O_3) \quad (5)$$

235   **2.4 Empirical Kinetic Modelling Approach**

236   The empirical kinetic modelling approach (EKMA) used in this work is a set of imaginary

237   tests to reveal the dependence of photochemical oxidation products on the change in precursors.

238   We set up 30 × 30 matrices by reducing or increasing the measured VOCs and NOx

239   concentrations in the model input. The resulting radical concentrations and ozone production

240   rates were calculated correspondingly.

241   At this stage, the observed VOCs were grouped into different lumped species according

242   to their RACM2 classification; more details can be found in a previous publication (Tan et al.,
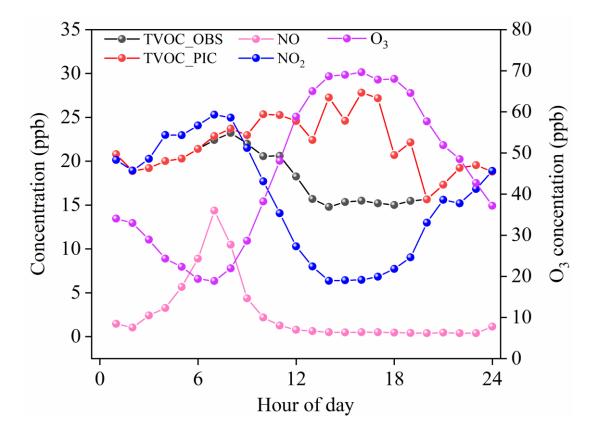
243 2017). The chemical model simulated photochemical reactions with input species for a time

244 interval of 60 minutes, which was enough for NOx, OH, HO_2, and RO_2 to reach a steady state

245 because the typical relaxation time of the chemical system is 5-10 minutes in summer (Tan et

246 al., 2018). However, all the species and parameters were input at a 5 min interval by data

247 interpolation to reduce simulation inconsistencies and large distortions of meteorological

248 parameters at longer time intervals (Tan et al., 2018). The ozone production rate was calculated

249 as described in Sect. 2.3. It is worth mentioning that the average survey data were selected as

250 the baseline scenario in simulating the EKMA curve in this study.

3. Results and discussion

251

3.1 Overview of diurnal variation in O_3, NOx, and TVOC

252

253 Figure 1 shows the average diurnal variation of concentrations in O_3, NOx, and TVOC

254 (including alkanes, alkenes, OVOCs, and halohydrocarbons) driven by emissions,

255 photochemical reactions and the evolution of the mixing layer height (MLH). The ozone

256 concentration during the observation period was 44.8±27.2 ppb with a maximum of 119.1 ppb,

257 as reported in our previous study (Zhan et al., 2021), which was generally comparable with the

258 O_3 concentrations during 2014-2018 (Ma et al., 2020). The O_3 followed a unimodal curve with

259 a minimum value (18.8±15.4 ppb) at 07:00 and then it increased to a maximum value (69.6

260 ppb) at 15:00 as photochemical ozone formed. In contrast, NOx reached its maximum

261 concentration (39.7±14.2 ppb) at 07:00 and then decreased. After 07:00, the mixing ratio of

262 NO continuously dropped, while the concentration of NO_2 decreased at first and then started

263 to increase at 14:00. The diurnal variations in the observed TVOCs were generally consistent

264   with those of NO_2. The observed TVOCs concentrations ranged from 2.2 to 23.2 ppb, with a

265   mean value of 18.6±2.6 ppb. Compared to the concentrations (45.4±15.2 ppb) in the same

266   period in August 2015 (Li et al., 2016a), the concentration of VOCs in Beijing was effectively

267   reduced. However, the photochemical initial concentrations (PICs) of TVOCs, which varied

268   from 2.2 to 27.8 ppb with a mean value of 24.5±2.1 ppb, showed a different diurnal curve

269   compared with the observed concentrations. It slightly increased from 07:00 to 14:00, which

270   was similar to the diurnal variation of VOCs in previous work (Zhan et al., 2021). The average

271   PIC-VOCs was 6.9±0.5 ppb higher than the observed concentration of TVOCs, indicating an

272   underestimated contribution of the local photochemistry of VOCs to O_3 and organic aerosol

273   formation.

274

275   **Figure. 1.** Overview of average diurnal variations in O_3, NOx, and TVOC. The data represent

276   measured results, except for those of the TVOC_PIC, which are calculated based on OH radical

14

277   exposure. The data range is August 1-28, 2019.

278   **3.2 Influence of photochemical loss of VOCs on the O_3 formation sensitivity regime**

279   The sensitivity of O_3 formation is analysed using the isopleth diagram generated from the

280   EKMA model, which is widely used to qualitatively study O_3-NOx-VOCs sensitivity. As

281   described in Sect. 2.4, the concentrations of NO_2 and VOCs were artificially scaled to $\pm 75\%$

282   of the observed values to calculate the response of O_3 concentration to an imaginary change in

283   the concentrations of NO_2 and VOC, with other constrained conditions remaining unchanged.

284   Figure 2 shows the typical EKMA curves during our observations. The black stars and

285   pentagons denote the observed concentrations of NOx and VOCs in the morning (09:00-10:00)

286   and at noon (14:00-15:00), respectively, while the blue symbols are the corresponding values

287   of PICs. Based on the measured data, O_3 formation was in a VOC-limited regime in the

288   morning and a NOx-limited regime in the afternoon. The black arrow indicates a linearly

289   decreasing trend of NOx and VOCs from 09:00 to 15:00 in the chemical coordinate system,

290   and ozone production shifted from VOC-limited to NOx-limited conditions from morning to

291   afternoon, which was consistent with the mean diurnal profiles (Figure 1). This was similar to

292   the data reported in Wangdu (Tan et al., 2018). As expected, ozone production shifted from a

293   VOC-limited regime (the observed VOCs) to a transition regime based on the PIC-VOCs in

294   the morning. Ozone production clearly moved further to a NOx-limited regime in the afternoon

295   after the photochemically consumed NOx and VOCs had been accounted for (Figure 2).

296   Because the average photochemical ageing time was only 1.7 ± 0.9 h, these results indicated

297   that the O_3 formation mechanism might typically be misdiagnosed, which misleads mitigation

298   measures for O_3 prevention if the consumed VOCs under real atmospheric conditions are not
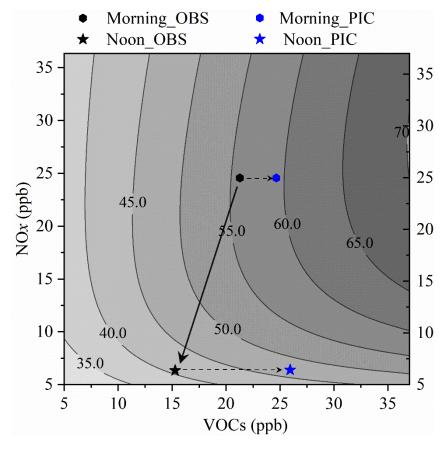
299   considered.

300

301   **Figure 2.** Isopleth diagram of the ozone concentration as a function of the concentration of

302   NOx and VOCs derived from an empirical kinetic modelling approach. The pentagons and stars

303   indicate the status in the morning (09:00-10:00) and at noon (14:00-15:00), respectively. The

304   black and blue colours represent the observed and corrected statuses, respectively.

305   **3.3 Contribution of VOC species to O_3 production**

306   The time series of simulated OH, HO_2, and RO_2 concentrations were used to calculate the

307    $P(O_3)$ and $L(O_3)$. The diurnally averaged $P(O_3)$ and $L(O_3)$ are shown in Figure 3. Ozone

308   formation can be divided into processes related to RO_2+NO and HO_2+NO (Sect. 2.3).

309   According to their VOC precursors, peroxyl radical groups were divided into alkane-derived

310 (ALKAP), alkene-derived (ALKEP), aromatic-derived (AROMP), isoprene-derived (ISOP),

311 oxygenated-VOC-derived (OVOCP), and halohydrocarbon-derived (HALOP) RO_2 and HO2P.

312 The ozone destruction processes included the reaction between O_3 and HOx (O3D1), the

313 reaction between O1D and H_2O (O3D2), the reaction between O_3 and alkenes (O3D3), and the

314 reaction between NO_2 and OH (O3D4).

315   Based on the observed VOCs (or PIC-VOCs), a fast O_3 production rate was observed at

316 14:00 (or 13:00), with a diurnal maximum value of 16.1 (or 25.6) ppb h^{-1} (Figure 3a and 3b),

317 while the peak destruction rate was 6.4 (or 8.6) ppb h^{-1} at 15:00 (or 13:00) (Figure 3c and 3d).

318 The average daytime $P(O_3)$ from 07:00 to 19:00 based on the initial concentrations of VOCs

319 was 4.0±3.1 ppb h^{-1} higher than that based on the measured VOCs concentrations (Figure 3b).

320 At the same time, the $F(O_3)$ from 07:00 to 19:00 based on the initial concentrations of VOCs

321 was also 3.0±2.1 ppb h^{-1} higher than the measured counterpart (Figure S12). Thus, the net O_3

322 production could be accumulatively underestimated by ~36 ppb day^{-1} from 07:00 to 19:00 if

323 the consumption of VOCs was not considered. This meant that the contribution of the local

324 formation of O_3 could be underestimated using the directly measured VOCs concentrations. It

325 should be pointed out that it is better to compare O_3 production with the true metric for O_3

326 production. However, it is impossible to directly measure the true metric for O_3 production in

327 the atmosphere at the present time to know how well the method presented here corrects for

328 that underestimation. In addition, the ozone concentrations must be constrained when

329 simulating the ozone formation process (Lu et al., 2013; Tan et al., 2017). Thus, it is impossible

330 to directly compare the ozone production based on PIC-VOCs with that using measured VOCs

331　concentrations. Therefore, we alternatively compared the integrated net ozone production rates

332　rather than ozone production or concentrations between the two scenarios. An upwind O_3 and

333　VOCs measurement combined with a trajectory analysis might provide an approach for

334　checking the accuracy of our results. Alternatively, conducting a transient O_3 production rate

335　analysis after subtracting the transport of O_3 with a regional model and/or satellite observation

336　might be another option. Unfortunately, neither the upwind measurement nor the regional

337　model simulation was available at the time of our study. To further check the accuracy of our

338　results, we chose August 4th as a test case to explore the influence of the transport of ozone on

339　a downwind site based on the trajectory analysis. As shown in Figure S13, the mean ozone

340　concentration of the downwind site (national monitoring station, NMS) was 27.6±21.9 ppb

341　day^{-1} higher than that of the observation site (OS), which was slightly less than the difference

342　(~36 ppb day^{-1}) between PIC-VOCs and observed VOCs and indirectly rationalized our results.

343　　　The HO_2 path contributed 64.8% to the total ozone formation on average, which was

344　slightly higher than the reported value (57.0%) in Wangdu (Tan et al., 2018), whereas the RO_2

345　path, in which aromatics (9.4%), alkenes (8.4%), isoprene (7.8%), alkanes (4.7%), OVOCs

346　(4.3%) and halohydrocarbons (0.6%) were the main contributors, contributed to the remaining

347　part. For the PIC-VOCs, the dominant path of O_3 production (51.7%) was still the HO_2 path,

348　followed by the RO_2 path related to alkenes (14.7%), aromatics (12.8%), and isoprene (11.7%).

349　The relative contribution of the RO_2 path to $P(O_3)$ increased by 13.4% compared with the

350　measured VOCs, particularly alkene-derived RO_2, which increased by 10.2%. As shown in

351　Figure 3c and 3d, the destruction of total oxidants was dominated by the reaction between O_3

352 and alkenes (O3D3) in the morning. It gradually shifted to the reaction between NO_2 and OH

353 (O3D4) from 11:00 to 16:00 and the photolysis of O_3 followed by a reaction with water (O3D2)

354 from 12:00 to 15:00 because O_3 concentration increased while NO_2 decreased (Figure 3c).

355 Figure S14 shows the percentages of the different paths of $P(O_3)$ and $L(O_3)$. The relative

356 contributions of the reactions between O_3 and alkenes (O1D3) and between NO_2 and OH

357 (O1D4) to the O_3 sinks decreased when calculated based on PIC-VOCs compared with those

358 of the measured VOCs, while they obviously increased for the other two paths, i.e., O3D1 and

359 O3O2. The O_3 destruction of the HOx and O_3 reaction (O3D1) gradually increased with the

360 continuous photochemical reaction. In addition, the maximum O_3 formation rates of the RO_2

361 derived from OVOCs and halohydrocarbons were 0.75 and 0.18 ppb h^{-1}, respectively. These

362 values could be underestimated due to the incomplete gas reaction mechanism of OVOCs and

363 halohydrocarbons in MCM3.3.1. In general, the measured VOCs as model inputs could fail to

364 truly reflect the oxidation capacity and underestimate the local formation of O_3 and organic

365 aerosols (Zhan et al., 2021).
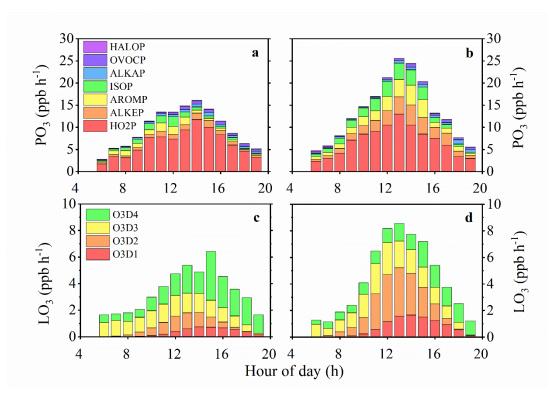
Figure 3. Mean diurnal profile of the instantaneous ozone production and destruction rate

calculated from the MCM-OBM model (instantaneous ozone rate derived from observed VOCs

in a and c and from PIC-VOCs in b and d). The upper panel presents the speciation of the ozone

formation rate. The lower panel presents the speciation of the ozone destruction rate. The data

range is August 1-28, 2019.

The budget of OH-HO_2-RO_2 radicals was further analysed to understand the

photochemical O_3 formation process. The comparison of the radical budget derived from the

observed and PIC-VOCs is shown in Figure 4. The radical cycles are divided into radical

sources (green boxes), radical sinks (black boxes), radical propagations (red circles) and

equilibria between radical and reservoir species (yellow boxes). The numbers or percentages

are the average formation rates (ppb h^{-1}) or relative contributions of the corresponding reaction

path based on the observed VOCs (outside the brackets) and the PIC-VOCs (inside the brackets)

380 to a certain radical. The relative contributions of different radical paths based on the observed

381 VOCs (outside the brackets) were comparable with those reported in Beijing, Shanghai, and

382 Guangzhou (Tan et al., 2019), while variations were observed for some reaction paths based

383 on the PIC-VOCs. For example, the reaction between ozone and alkenes based on initial VOC

384 concentrations (percentages inside the brackets) contributed more to OH (from 7% to 21%)

385 and HO_2 radical production (from 6% to 12%), while photolysis of HONO and HCHO

386 contributed less to the production of OH (from 76% to 60%) and HO_2 radicals (from 44% to

387 40%), respectively. Other radical sources were consistent between the two scenarios.

388 Interestingly, the average formation rates of OH, HO_2 and RO_2 radicals derived from the PIC-

389 VOCs were obviously higher than those from the observed VOCs. In particular, the oxidation

390 of NO by RO_2 and HO_2 increased by 1.6 and 1.3 ppb h^{-1}, respectively. The enhanced oxidation

391 rate of NO was equal to the increase in the average $F(O_3)$ in the analysis process above. This

392 meant that the radical propagation of $OH-RO_2-HO_2$ sped up in the case of PIC-VOCs,

393 subsequently accelerating the chemical loop of $NO-NO_2-O_3$. For the radical sinks and equilibria

394 related to HNO_4, $RONO_2$ and PAN, the values were basically comparable between the two

395 scenarios. In addition, the O_3 formation from the RO_2 path increased by 4.1% (from 39.5% to

396 43.6%) in the simulation using the PIC-VOCs compared with the observed VOCs. The above

397 budget analysis explained the observed increases in $F(O_3)$ (~3 ppb h^{-1}), which were mainly

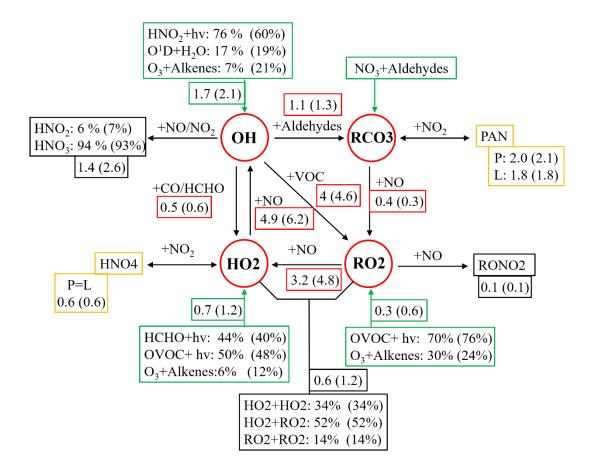398 driven by the reaction of missed reactive VOCs, such as alkenes, with O_3.

Figure 4. Comparison of the OH-HO$_2$-RO$_2$ radical budget derived from the observed and PIC-VOCs under daytime conditions (07:00 to 19:00 LT). The green, black, red and yellow boxes denote the sources of radicals, radical sinks, radical propagation, and racial equilibrium, respectively. The numbers or percentages outside and inside the brackets are the average formation rates (ppb h^{-1}) or relative contributions to a specific radical of the corresponding reaction path based on observed VOCs and PIC-VOCs, respectively.

3.4 In situ O$_3$ formation process

In addition to chemical processes, which can be simulated using the OBM-MCM model, transport processes, including horizontal, vertical transportation and dry deposition processes (Tan et al., 2019), also have an important influence on the O$_3$ concentration. Thus, the change in instantaneous ozone concentration can reflect the combined effect between photochemical

411   and physical transport processes (Tan et al., 2019). This change can be expressed as,

412    $$\frac{dO_x}{dt} = F(O_3) + R(O_3) \quad (6)$$

413   where dOx/dt is the O_3 concentration change rate based on the measured data (ppb h^{-1}); $F(O_3)$

414   is the net O_3 formation rate (ppb h^{-1}), and $R(O_3)$ indicates transportation (ppb h^{-1}). A positive

415   value of $R(O_3)$ indicates an inflow of O_3 with airmass and vice versa. O_3 was replaced with Ox

416   (O_3+NO_2) to correct the titration of O_3 by NO (Pan et al., 2015).

417

418   **Fig. 5.** The variation in Ox concentration and formation rate during an O_3 pollution episode

419   (Aug. 1st). (a and b present the local ozone formation processes of the measured and PIC-VOCs,

420   respectively.)

421   The O_3 budget analysis was performed during an O_3 pollution episode (Aug. 1st). Figure

422   5 shows the simulated local ozone formation process based on the measured and PIC-VOCs.

423   The hourly variation in O_3 concentrations from 19:00 to 6:00 the next day was dominated by

424   regional transportation without O_3 formation, while local photochemical O_3 formation could

425   explain all or part of the O_3 concentration change during the time window from 07:00 to 19:00.

426   The $d(O_3)/dt$ shows an increase from 07:00 to 15:00 LT. However, $d(O_3)/dt$ sharply changed to

427   negative values at 16:00, which was consistent with diurnal O_3 (the O_3 peaks at 15:00) in Figure

428   1.

429   The average daytime $F(O_3)$ based on the observed and photochemical initial

430   concentrations was 6.4±4.0 and 8.9±6.7 ppb h^{-1}, respectively. Photochemical O_3 formation

431   under both conditions started at 07:00 and reached maximum values of 12.6 and 19.6 ppb h^{-1}

432   at 15:00, respectively. The maximum daily value of $P(O_3)$ was higher than those in the urban

433   areas of Japan, America, and England (Whalley et al., 2018; Ren et al., 2006; Griffith et al.,

434   2016; Kanaya et al., 2009) and lower than those in the suburbs of Guangzhou (Lu et al., 2012)

435   and the urban areas and suburbs of Beijing (Lu et al., 2013). Before 12:00, the O_3 formation

436   rate based on the PIC-VOCs was slightly higher than that based on the measured VOCs, while

437   both rates were within a range of 2.0~6.5 ppb h^{-1}. From 12:00 to 17:00, the O_3 formation rate

438   based on the PIC-VOCs and the observed concentration of VOCs greatly increased due to

439   active photochemistry.

440   As shown in Figure 5, the increased O_3 concentration was larger than the local O_3

441   photochemical production from 07:00 to 12:00 ($R(O_3)$ was positive). This was mainly because,

442   under stable conditions, the nighttime residual layer (RL) is isolated from mixing with the

443   nighttime surface layer (Tan et al., 2021). The RL layer usually contains an air mass with a

444   higher ozone mixing ratio than in the surface layer. In the morning, surface heating causes

445   mixing upward in the surface layer until the temperature inversion is eroded away and rapid

446   mixing of pollutants throughout the surface and boundary layer occurs. However, $R(O_3)$ was

447   negative in the afternoon, which indicated that the local O_3 formation at the measurement site

448   contributed to not only the changes in the in situ O_3 concentration but also the O_3 source of the

449   downwind regions. This was more clearly shown in Figure 4B under the PIC-VOCs condition.

450   These results illustrated that local O_3 photochemistry played a crucial role in both the local and

451   regional O_3 concentrations, which can be underestimated if consumed VOCs with high

452   reactivities are ignored.

453   **4. Conclusions**

454   In this study, we presented the local O_3 formation process in August 2019 in Beijing based

455   on the concentrations of observed and PIC-VOCs. The mean diurnal profile of O_3 was

456   unimodal with a peak at 15:00, while NOx and observed TVOCs showed an opposite diurnal

457   curve, and the PICs of TVOCs showed a different diurnal curve compared with that of the

458   observed VOCs, with a slight increase from 07:00 to 14:00. The EKMA curve indicated that

459   instantaneous O_3 production was dependent on the real-time concentrations of NOx and VOCs,

460   i.e., the VOC-limited regime in the morning (09:00-10:00) and the NOx-limited regime at noon

461   (14:00-15:00). The sensitivity regime of O_3 formation could be misdiagnosed if the consumed

462   VOCs are not considered, for example, the VOC-limited regime (observed) shift to a transition

463   regime (PIC-VOCs) in the morning is ignored. The mean $F(O_3)$ based on PIC-VOCs was 3.0

464   ppb h^{-1} higher than that based on the measured VOCs, indicating that the underestimation of

465   local photochemistry in the local O_3 concentration could reach ~36 ppb day^{-1} if the consumed

466   VOCs are not accounted for. And the mean ozone concentration of downwind site was 27.6

467   ppb day^{-1} higher than the observation site, slightly lower than the difference (~36 ppb day^{-1})

468   between PIC-VOCs and observed VOCs, which indirectly supported the accuracy of the above

469   results. The radical budget analysis explained the observed increases in $F(O_3)$ (3 ppb h^{-1}), which

470   were mainly driven by the reaction of missed reactive VOCs, such as alkenes, with O_3. In

471   addition, the OH-HO$_2$ radical cycle was obviously accelerated by highly reactive alkenes after

472   the photochemical loss of VOCs was accounted for. Finally, the results of the in situ O_3

473   formation process indicated that local O_3 photochemical formation played a key role in both

474   local and regional O_3 concentrations. In conclusion, our results suggested that PIC-VOCs were

475   more suitable than the observed VOC concentrations for diagnosing O_3 formation sensitivity.

476

477   **Author contributions:** Wei Ma: Methodology, data curation, and writing of the original draft;

478   Zemin Feng: Methodology, investigation, data curation, and writing of the original draft; Junlei

479   Zhan: Methodology, investigation, data curation; Yongchun Liu: Conceptualization,

480   investigation, data curation, writing, reviewing & editing, supervision, and funding acquisition;

481   Pengfei Liu: Methodology, investigation, data curation, writing, reviewing & editing;

482   Chengtang Liu: Methodology, investigation, data curation, writing, reviewing & editing;

483   Qingxin Ma: Methodology, investigation, data curation; Kang Yang: Methodology,

484   investigation, data curation. Yafei Wang: Methodology, investigation, resources, data curation;

485   Hong He: Resources, writing, reviewing & editing; Markku Kulmala: Methodology, writing,

486   reviewing & editing; Yujing Mu: Conceptualization, methodology, data curation, writing,

487   reviewing & editing. Junfeng Liu: Conceptualization, methodology, data curation, writing,

488   reviewing & editing, and supervision.

489   **Competing interests:** The authors declare that they have no substantive conflicts of interest.

490   **Data availability:** Data are available upon request to Yongchun Liu (liuyc@buct.edu.cn).

496

497

Reference

Atkinson, R. and Arey, J.: Atmospheric degradation of volatile organic compounds, Chemical Reviews, 103, 4605-4638, https://doi.org/10.1021/cr0206420, 2003.

Carter, W. P. L.: Development of Ozone Reactivity Scales for Volatile Organic Compounds.   1994a, J. Air Waste Manage. Assoc., 44, 881-899, https://doi.org/10.1080/1073161X.1994.10467290, 1994.

Chen, T., Liu, J., Liu, Y., and Ma, Q. G., Yanli; Zhong,Cheng; Jiang,Haotian; Chu,Biwu; Zhang,Peng; Ma,Jinzhu; Liu,Pengfei; Wang,Yafei; Mu,Yujing; He,Hong: Chemical characterization of submicron aerosol in summertime Beijing: A case study in southern suburbs in 2018, Chemosphere, 247, 125918, https://doi.org/10.1016/j.chemosphere.2020.125918, 2020.

Cohen, A. J., Brauer, M., Burnett, R., and Anderson, H. R. F., Joseph; Estep,Kara; Balakrishnan,Kalpana; Brunekreef,Bert; Dandona,Lalit; Dandona,Rakhi; Feigin,Valery; Freedman,Greg; Hubbell,Bryan; Jobling,Amelia; Kan,Haidong; Knibbs,Luke; Liu,Yang; Martin,Randall; Morawska,Lidia; Pope,C. Arden, III; Shin,Hwashin; Straif,Kurt; Shaddick, Gavin; Thomas,Matthew; van Dingenen,Rita; van Donkelaar,Aaron; Vos,Theo; Murray,Christopher J. L; Forouzanfar,Mohammad H.: Estimates and 25-year trends of the global burden of disease attributable to ambient air pollution: an analysis of data from the Global Burden of Diseases Study 2015, Lancet, 389, 1907-1918, https://doi.org/10.1016/s0140-6736(17)30505-6, 2017.

Dang, R. and Liao, h.: Radiative Forcing and Health Impact of Aerosols and Ozone in China as the Consequence of Clean Air Actions over 2012–2017, J Geophysical Research Letters, 46, 12511-12519, https://doi.org/10.1029/2019GL084605, 2019.

Feng, Z., De Marco, A., Anav, A., Gualtieri, M., Sicard, P., Tian, H., Fornasier, F., Tao, F., Guo, A., and Paoletti, E.: Economic losses due to ozone impacts on human health, forest productivity and crop yield across China, Environment International, 131, 104966, https://doi.org/10.1016/j.envint.2019.104966, 2019.

Gao, J., Zhang, J., Li, H., Li, L., and Xu, L. Z., Yujie; Wang,Zhanshan; Wang,Xuezhong; Zhang,Weiqi; Chen,Yizhen; Cheng,Xi; Zhang,Hao; Peng,Liang; Chai,Fahe; Wei,Yongjie: Comparative study of volatile organic compounds in ambient air using observed mixing ratios and initial mixing ratios taking chemical loss into account - A case study in a typical urban area in Beijing, Science of the Total Environment, 628-629, 791-804, https://doi.org/10.1016/j.scitotenv.2018.01.175, 2018.

Gao, Y., Li, M., Wan, X., Zhao, X., Wu, Y., Liu, X., and Li, X.: Important contributions of alkenes and aromatics to VOCs emissions, chemistry and secondary pollutants formation at an industrial site of central eastern China, Atmospheric Environment, 244, 117927, https://doi.org/10.1016/j.atmosenv.2020.117927, 2021.

Goldan, P. D., Parrish, D. D., Kuster, W. C., Trainer, M., Mckeen, S. A., Holloway, J., Jobson, B. T., Sueper, D. T., and Fehsenfeld, F. C.: Airborne measurements of isoprene, CO, and anthropogenic hydrocarbons and their implications, Journal of Geophysical Research-Atmospheres, 105, 9091-9105, http://doi.org/10.1029/1999JD900429, 2000.

Griffith, S. M., Hansen, R. F., Dusanter, S., Michoud, V., Gilman, J. B., Kuster, W. C., Veres, P. R., Graus, M., de Gouw, J. A., Roberts, J., Young, C., Washenfelder, R., Brown, S. S., Thalman, R., Waxman, E., Volkamer, R., Tsai, C., Stutz, J., Flynn, J. H., Grossberg, N., Lefer, B., Alvarez, S. L., Rappenglueck, B., Mielke, L. H., Osthoff, H. D., and Stevens, P. S.: Measurements of hydroxyl and hydroperoxy radicals during CalNex-LA: Model comparisons and radical budgets, Journal of Geophysical Research-Atmospheres, 121, 4211-4232, https://doi.org/10.1002/2015jd024358, 2016.

Han, D., Wang, Z., Cheng, J., Wang, Q., Chen, X., and Wang, H.: Volatile organic compounds (VOCs) during

non-haze and haze days in Shanghai: characterization and secondary organic aerosol (SOA) formation, Environmental Science and Pollution Research, 24, 18619-18629, https://doi.org/10.1007/s11356-017-9433-3, 2017.

He, Z., Wang, X., Ling, Z., Zhao, J., Guo, H., Shao, M., and Wang, Z.: Contributions of different anthropogenic volatile organic compound sources to ozone formation at a receptor site in the Pearl River Delta region and its policy implications, Atmospheric Chemistry and Physics, 19, 8801-8816, https://doi.org/10.5194/acp-19-8801-2019, 2019.

Jobson, B. T., Berkowitz, C. M., Kuster, W. C., Goldan, P. D., Williams, E. J., Fesenfeld, F. C., Apel, E. C., Karl, T., Lonneman, W. A., and Riemer, D.: Hydrocarbon source signatures in Houston, Texas: Influence of the petrochemical industry, Journal of Geophysical Research-Atmospheres, 109, http://doi.org/10.1029/2004jd004887, 2004.

Kanaya, Y., Pochanart, P., Liu, Y. L., J;, Tanimoto, H., Kato, S., Suthawaree, J., Inomata, S., Taketani, F., Okuzawa, K., Kawamura, K., Akimoto, H., and Wang, Z. F.: Rates and regimes of photochemical ozone production over Central East China in June 2006: a box model analysis using comprehensive measurements of ozone precursors, Atmospheric Chemistry and Physics, 9, 7711-7723, https://doi.org/10.5194/acp-9-7711-2009, 2009.

Li, J., Wu, R., Li, Y., Hao, Y., and Xie, S. Z., Liming;: Effects of rigorous emission controls on reducing ambient volatile organic compounds in Beijing, China, Science of the Total Environment, 557, 531-541, https://doi.org/10.1016/j.scitotenv.2016.03.140, 2016a.

Li, J., Yang, W., Wang, Z., Chen, H., Hu, B., Li, J., Sun, Y., Fu, P., and Zhang, Y.: Modeling study of surface ozone source-receptor relationships in East Asia, Atmospheric Research, 167, 77-88, https://doi.org/10.1016/j.atmosres.2015.07.010, 2016b.

Li, L., An, J. Y., Shi, Y. Y., and Zhou, M. Y., R. S; Huang, C; Wang, H. L; Lou, S. R; Wang, Q; Lu, Q; Wu, J.: Source apportionment of surface ozone in the Yangtze River Delta, China in the summer of 2013, Atmospheric Environment, 144, 194-207, https://doi.org/10.1016/j.atmosenv.2016.08.076, 2016c.

Li, M., Zhang, Q., Zheng, B., Tong, D., Lei, Y., Liu, F., Hong, C., Kang, S., Yan, L., Zhang, Y., Bo, Y. S., Hang;, Cheng, Y., and He, K.: Persistent growth of anthropogenic non-methane volatile organic compound (NMVOC) emissions in China during 1990-2017: drivers, speciation and ozone formation potential, Atmospheric Chemistry and Physics, 19, 8897-8913, https://doi.org/10.5194/acp-19-8897-2019, 2019.

Ling, Z. H. and Guo, H.: Contribution of VOC sources to photochemical ozone formation and its control policy implication in Hong Kong, Environmental Science & Policy, 38, 180-191, https://doi.org/10.1016/j.envsci.2013.12.004, 2014.

Liu, J., Li, X., Tan, Z., Wang, W., and Zhang, Y.: Assessing the Ratios of Formaldehyde and Glyoxal to NO_2 as Indicators of O_3–NOx–VOC Sensitivity, Environmental Science Technology, 55, 10935-10945, https://doi.org/10.1021/acs.est.0c07506, 2021.

Liu, Y., Yan, C., Feng, Z., Zheng, F., and Kulmala, M.: Continuous and comprehensive atmospheric observations in Beijing: a station to understand the complex urban atmospheric environment, Big Earth Data, 4, 295-321, https://doi.org/10.1080/20964471.2020.1798707, 2020a.

Liu, Y., Ni, S., Jiang, T., Xing, S., Zhang, Y., Bao, X., Feng, Z., Fan, X., Zhang, L., and Feng, H.: Influence of Chinese New Year overlapping COVID-19 lockdown on HONO sources in Shijiazhuang, Science of the Total Environment, 745, 141025, https://doi.org/10.1016/j.scitotenv.2020.141025, 2020b.

Liu, Y., Zhang, Y., Lian, C., Yan, C., Feng, Z., Zheng, F., Fan, X., Chen, Y., Wang, W., Chu, B., Wang, Y., Cai, J., Du, W., Daellenbach, K. R., Kangasluoma, J., Bianchi, F., Kujansuu, J., Petaja, T., Wang, X., Hu, B., Wang, Y.,

Ge, M., He, H., and Kulmala, M.: The promotion effect of nitrous acid on aerosol formation in wintertime in Beijing: the possible contribution of traffic-related emissions, Atmospheric Chemistry and Physics, 20, 13023-13040, https://doi.org/10.5194/acp-20-13023-2020, 2020c.

Lu, K. D., F. Rohrer; F. Holland, H. F., B. Bohn,T. Brauers,C. C. Chang,R. Haseler ,M. Hu,K. Kita, and , Y. K., X. Li,S. R. Lou,S. Nehr,M. Shao,L. M. Zeng,A. Wahner,Y. H. Zhang,and A. Hofzumahaus: Observation and modelling of OH and HO2 concentrations in the Pearl River Delta 2006: a missing OH source in a VOC rich atmosphere, Atmospheric Chemistry and Physics, 12, 1541-1569, https://doi.org/10.5194/acp-12-1541-2012, 2012.

Lu, K. D., Hofzumahaus, A., Holland, F., Bohn, B., Brauers, T., Fuchs, H., Hu, M., Haeseler, R., Kita, K., Kondo, Y., Li, X., Lou, S. R., Oebel, A., Shao, M., Zeng, L. M., Wahner, A., Zhu, T., Zhang, Y. H., and Rohrer, F.: Missing OH source in a suburban environment near Beijing: observed and modelled OH and HO_2 concentrations in summer 2006, Atmospheric Chemistry and Physics, 13, 1057-1080, https://doi.org/10.5194/acp-13-1057-2013, 2013.

Lu, X., Chen, N., Wang, Y., Cao, W., Zhu, B., Yao, T., Fung, J. C. H., and Lau, A. K. H.: Radical budget and ozone chemistry during autumn in the atmosphere of an urban site in central China, Journal of Geophysical Research-Atmospheres, 122, 3672-3685, https://doi.org/10.1002/2016jd025676, 2017.

Ma, j. K., Jyoti;, Li, V. O. K., and Lam, J. C. K.: Effects of China's current Air Pollution Prevention and Control Action Plan on air pollution patterns, health risks and mortalities in Beijing 2014-2018, Chemosphere, 260, 127572, https://doi.org/10.1016/j.chemosphere.2020.127572, 2020.

Ma, Z., Liu, C., Zhang, C., Liu, P., Ye, C., Xue, C., Zhao, D., Sun, J., Du, Y., Chai, F., and Mu, Y.: The levels, sources and reactivity of volatile organic compounds in a typical urban area of Northeast China, Journal of Environmental Sciences, 79, 121-134, https://doi.org/10.1016/j.jes.2018.11.015, 2019.

Mckeen, S. A., Liu, S. C., Hsie, E. Y., Lin, X., Bradshaw, J. D., Smyth, S., Gregory, G. L., and Blake, D. R.: Hydrocarbon ratios during PEM-WEST A: A model perspective, Journal of Geophysical Research: Atmospheres, 101, 2087-2109, https://doi.org/10.1029/95JD02733, 1996.

Monks, P. S.: Gas-Phase Radical Chemistry in the Troposphere, Chemical Society Reviews, 34, 376-395, https://doi.org/10.1039/B307982C, 2005.

Pan, X., Kanaya, Y., Tanimoto, H., Inomata, S., Wang, Z., Kudo, S., and Uno, I.: Examining the major contributors of ozone pollution in a rural area of the Yangtze River Delta region during harvest season, Atmospheric Chemistry and Physics, 15, 6101-6111, https://doi.org/10.5194/acp-15-6101-2015, 2015.

Ren, X., Brune, W. H., Mao, J., Mitchell, M. J., Lesher, R. L., Simpas, J. B., Metcalf, A. R., Schwab, J. J., Cai, C., Li, Y., Demerjian, K. L., Felton, H. D., Boynton, G., Adams, A., Perry, J., He, Y., Zhou, X., and Hou, J.: Behavior of OH and HO2 in the winter atmosphere in New York city, Atmospheric Environment, 40, S252-S263, https://doi.org/10.1016/j.atmosenv.2005.11.073, 2006.

Seinfeld, J. H. and Pandis, S. N.: Atmospheric chemistry and physics : from air pollution to climate change (Second Edition), 2006.

Shao, M., Wang, B., Lu, S., Yuan, B., and Wang, M.: Effects of Beijing Olympics Control Measures on Reducing Reactive Hydrocarbon Species, Environmental Science & Technology, 45, 514-519, https://doi.org/10.1021/es102357t, 2011.

Tan, Z., Fuchs, H., Lu, K., and Hofzumahaus, A. B., Birger; Broch,Sebastian; Dong,Huabin; Gomm,Sebastian; Haeseler,Rolf; He,Lingyan; Holland,Frank; Li,Xin; Liu,Ying; Lu,Sihua; Rohrer,Franz; Shao,Min; Wang,Baolin; Wang,Ming; Wu,Yusheng; Zeng,Limin; Zhang,Yinsong; Wahner,Andreas; Zhang,Yuanhang;: Radical chemistry

at a rural site (Wangdu) in the North China Plain: observation and model calculations of OH,HO$_2$ and RO$_2$ radicals, Atmospheric Chemistry and Physics, 17, 663-690, https://doi.org/10.5194/acp-17-663-2017, 2017.

Tan, Z., Lu, K., Jiang, M., Rong, S., and Zhang, Y.: Daytime atmospheric oxidation capacity in four Chinese megacities during the photochemically polluted season: A case study based on box model simulation, Atmospheric Chemistry Physics, 19, 3493-3513, https://doi.org/10.5194/acp-19-3493-2019, 2019.

Tan, Z., Lu, K., Jiang, M., Su, R., Dong, H., Zeng, L., Xie, S., Tan, Q., and Zhang, Y.: Exploring ozone pollution in Chengdu, southwestern China: A case study from radical chemistry to O$_3$-VOC-NOx sensitivity, Science of the Total Environment, 636, 775-786, https://doi.org/10.1016/j.scitotenv.2018.04.286, 2018.

Tan, Z. F., Ma, X. F., Lu, K. D., Jiang, M. Q., Zou, Q., Wang, H. C., Zeng, L. M., and Zhang, Y. H.: Direct evidence of local photochemical production driven ozone episode in Beijing: A case study, Science of the Total Environment, 800, http://doi.org/10.1016/j.scitotenv.2021.148868, 2021.

Wang, T., Xue, L., Brimblecombe, P., Lam, Y. F., Li, L., and Zhang, L.: Ozone pollution in China: A review of concentrations, meteorological influences, chemical precursors, and effects, Science of the Total Environment, 575, 1582-1596, https://doi.org/10.1016/j.scitotenv.2016.10.081, 2017.

Whalley, L. K., Stone, D., Dunmore, R., Hamilton, J., Hopkins, J. R., Lee, J. D., Lewis, A. C., Williams, P., Kleffmann, J., Laufs, S., Woodward-Massey, R., and Heard, D. E.: Understanding in situ ozone production in the summertime through radical observations and modelling studies during the Clean air for London project (ClearfLo), Atmospheric Chemistry and Physics, 18, 2547-2571, https://doi.org/10.5194/acp-18-2547-2018, 2018.

Wiedinmyer, C., Friedfeld, S., Baugh, W., Greenberg, J., Guenther, A., Fraser, M., and Allen, D.: Measurement and analysis of atmospheric concentrations of isoprene and its reaction products in central Texas, Atmospheric Environment, 35, 1001-1013, https://doi.org/10.1016/S1352-2310(00)00406-4, 2001.

Xie, Y., Dai, H., Zhang, Y., Wu, Y., Hanaoka, T., and Masui, T.: Comparison of health and economic impacts of PM2.5 and ozone pollution in China, Environment International, 130, 104881, https://doi.org/10.1016/j.envint.2019.05.075, 2019.

Xue, L. K., Wang, T., Gao, J., Ding, A. J., Zhou, X. H., Blake, D. R., Wang, X. F., Saunders, S. M., Fan, S. J., Zuo, H. C., Zhang, Q. Z., and Wang, W. X.: Ground-level ozone in four Chinese cities: precursors, regional transport and heterogeneous processes, Atmospheric Chemistry and Physics, 14, 13175-13188, https://doi.org/10.5194/acp-14-13175-2014, 2014.

Yang, Y., Shao, M., Kessel, S., Li, Y. L., Keding;, Lu, S. W., Jonathan;, Zhang, Y., Zeng, L., Noelscher, A. C., Wu, Y., Wang, X., and Zheng, J.: How the OH reactivity affects the ozone production efficiency: case studies in Beijing and Heshan, China, Atmospheric Chemistry and Physics, 17, 7127-7142, https://doi.org/10.5194/acp-17-7127-2017, 2017.

Yuan, B., Hu, W. W., Shao, M., Wang, M., Chen, W. T., Lu, S. H., Zeng, L. M., and Hu, M.: VOC emissions, evolutions and contributions to SOA formation at a receptor site in eastern China, Atmospheric Chemistry and Physics, 13, 8815-8832, https://doi.org/10.5194/acp-13-8815-2013, 2013.

Zhan, J., Feng, Z., Liu, P., He, X., He, Z., Chen, T., Wang, Y., He, H., Mu, Y., and Liu, Y.: Ozone and SOA formation potential based on photochemical loss of VOCs during the Beijing summer, Environmental Pollution, 285, 117444, https://doi.org/10.1016/j.envpol.2021.117444, 2021.

Zhang, K., Li, L., Huang, L., Wang, Y., Huo, J., Duan, Y., Wang, Y., and Fu, Q.: The impact of volatile organic compounds on ozone formation in the suburban area of Shanghai, Atmospheric Environment, 232, 117511, https://doi.org/10.1016/j.atmosenv.2020.117511, 2020.

Zhang, K., Huang, L., Li, Q., Huo, J., Duan, Y., Wang, Y., Yaluk, E., Wang, Y., Fu, Q., and Li, L.: Explicit modeling

665   of isoprene chemical processing in polluted air masses in suburban areas of the Yangtze River Delta region: radical

666   cycling and formation of ozone and formaldehyde, Atmospheric Chemistry and Physics, 21, 5905-5917,

667   https://doi.org/10.5194/acp-21-5905-2021, 2021a.

668   Zhang, M., Gao, W., Yan, J., Wu, Y., Marandino, C. A., Park, K., Chen, L., Lin, Q., Tan, G., and Pan, M.: An

669   integrated sampler for shipboard underway measurement of dimethyl sulfide in surface seawater and air,

670   Atmospheric Environment, 209, 86-91, https://doi.org/10.1016/j.atmosenv.2019.04.022, 2019.

671   Zhang, Q., Li, L., Zhao, W., Wang, X., Jiang, L., Liu, B., Li, X., and Lu, H.: Emission characteristics of VOCs

672   from forests and its impact on regional air quality in Beijing, China Environmental Science, 41, 622-632,

673   https://doi.org/10.19674/j.cnki.issn1000-6923.2021.0072, 2021b.

674   Zong, R. H., Xue, L. K., Wang, T. B., and Wang, W. X.: Inter-comparison of the Regional Atmospheric Chemistry

675   Mechanism (RACM2) and Master Chemical Mechanism (MCM) on the simulation of acetaldehyde, Atmospheric

676   Environment, 186, 144-149, http://doi.org/10.1016/j.atmosenv.2018.05.013, 2018.

677